Chemical Engineering Journal 401 (2020) 126058

Contents lists available at ScienceDirect

Chemical Engineering Journal

journal homepage: www.elsevier.com/locate/cej

Integrated effect of NH_2-functionalized/triazine based covalent organic framework black phosphorus on reducing fire hazards of epoxy nanocomposites

Shuilai Qiu[a,1], Bin Zou[a,1], Tao Zhang[a], Xiyun Ren[a], Bin Yu[b], Yifan Zhou[a], Yongchun Kan[a,*], Yuan Hu[a,*]

[a] State Key Laboratory of Fire Science, University of Science and Technology of China, 96 Jinzhai Road, Hefei, Anhui 230026, PR China
[b] Centre for Future Materials, University of Southern Queensland, Toowoomba 4300, Australia

HIGHLIGHTS

- The novel two-dimensional BP-NH-TOF hybrids was in situ synthesized.
- EP/ BP-NH-TOF exhibits low PHRR, THR, SPR, TSR and smoke toxicity.
- EP/BP-NH-TOF nanocomposites shows significantly enhanced mechanical property.
- Excellent fire safety and mechanical properties are owing to the P-N synergistic system.

ARTICLE INFO

Keywords:
Black phosphorus
Covalent organic framework
Composites
Mechanical properties
Fire hazards

ABSTRACT

As the most thermodynamical and chemical stable allotrope of phosphorus, black phosphorus (BP) has recently generated huge research interest due to its high carrier mobility, semi-conductive property and an intrinsically tunable bandgap. BP has shown potential application in flame retardant polymer nanocomposites as emerging nanofiller. However the utilization of BP in polymer nanocompsoites still remains a huge challenge as it is prone to oxidation in water under air condition and pristine BP shows limited flame retardancy efficiency. In order to solve these issues, herein, triazine based organic framework was grown onto the surface of two-dimensional (2D) BP by in situ polymerization, resulting in the formation of organic-inorganic hybrids (BP-NH-TOF) which were subsequently incorporated into epoxy resin to fabricate the final nanocomposites. With increasing the loading of BP-NH-TOF in EP nanocomposites, the corresponding PHRR, THR, TSR and SPR values were reduced remarkably. For example, the addition of 2 wt% BP-NH-TOF results in a maximum decrease in PHRR (61.2%) and THR (44.3%) along with the dramatically improved LOI (29.0%) and UL-94 (V-0) performance, in addition to the obvious reduction of the amount of toxic carbon monoxide and flammable volatile products. Meanwhile, the mechanical properties of EP/BP-NH-TOF nanocomposites are enhanced significantly, e.g. 67.1% improvement in storage modulus at 1 wt% of BP-NH-TOF loading along with the improved glass transition temperature. The outstanding fire safety and mechanical properties of EP nanocomposites are attributed to the synergistic action of BP-NH-TOF hybrids. This work provides a facile method to prepared functionlized BP with the application in high performance flame retardant polymer nanocomposites.

1. Introduction

Black phosphorus (BP) is emerging as the most stable allotrope of solid phosphorus in thermodynamics and chemistry[1], which has found potential applications in catalysis, energy and optoelectronic devices owing to its exceptional mechanical, electronic, optical and transport properties [2–5]. Recently, A puckered layer structure is integrated into bulk BP via weak van der Waals forces [6]. Exfoliation strategy is extensively explored to generate single- or few-layer two-dimensional (2D) BP nanosheets. After exfoliation of bulk BP, BP

* Corresponding authors.
E-mail addresses: yckan@ustc.edn.cn (Y. Kan), yuanhu@ustc.edu.cn (Y. Hu).
[1] Joint first author, these authors contributed equally to this work.

https://doi.org/10.1016/j.cej.2020.126058
Received 9 August 2019; Received in revised form 21 June 2020; Accepted 23 June 2020
Available online 26 June 2020

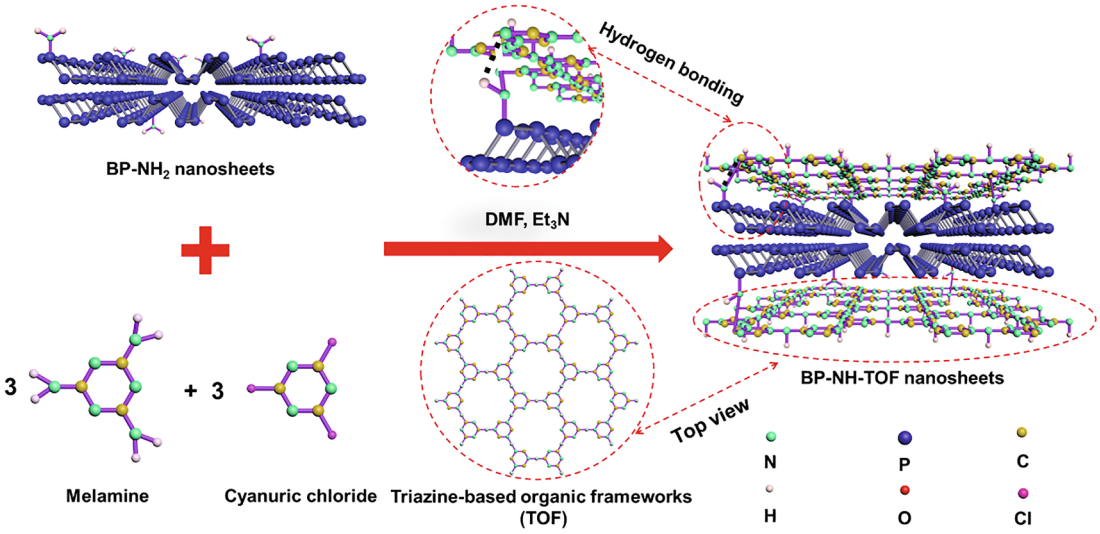

Fig. 1. Schematic illustration of the fabrication process of the BP-NH-TOF nanohybrids.

nanosheets possess high specific surface area and abundant active sites. Sonication-assisted liquid exfoliation is regarded as an effective strategy to prepare BP nanosheets [7,8] , but is usually time-consuming, environmentally harmful. More importantly, it is difficult to completely remove auxiliary organic solvents on the surface of BP nanosheets [9]. After liquid exfoliation, there are few active groups on the surface of BP, which can not provide active sites for further chemical functionalization due to its intrinsically inert nature. Recently, hydroxyl functionalized BP nanosheets have been achieved successfully by ball-milling mixing of BP power with LiOH [10]. In another work, $–NH_2$ functionalized BP nanosheets were synthesized via urea-assisted ball-milling [11]. These impressive results demonstrate that ball milling can realize simultaneous exfoliation and functionalization of bulk BP at large scale, which makes it possible for preparing BP-based functional materials.

Covalent organic frameworks (COFs) are a class of novel crystalline nanomaterial composed of a porous network structure, which have strong covalent bonds between organic moieties. Generally, COFs maintain two- or three-dimensional structures with the characteristics of regular porous, low density, high crystallinity and good stability. Up to now, various COFs have been developed, such as boronate esters [12,13], triazines [14,15], Schiff-base types, etc [16,17]. Owing to the huge species and unique characteristics, COFs have generated great interest in a variety of applications, such as catalysis, energy, optoelectronic devices and sensors [18–20]. However, it remains still a long-term challenge to explore different applications of COFs. Triazine based covalent organic frameworks (TOFs) fabricated from triazine or nitrile containing reactant by covalent bonding has been regarded as an important sub-class of COFs, due to their unique structure and characteristics of marvelous surface area, abundant nitrogen elements and high stability in organic media [21]. These attractive features enable TOFs to be used as promising nanofillers for polymeric materials with improved properties.

Because of increasing concerns in environmental persistence and bio-accumulation of halogenated flame retardants [22,23], phosphorus- and nitrogen-containing flame retardants are highly attractive for application in flame retardation of polymeric materials. As an important subset of synergistic flame retardant systems, phosphorus–nitrogen (P-N) synergistic action has been extensively explored due to their high efficiency in the past few decades [24]. Exploring and developing new highly efficient P-N synergistic flame retardant systems will be an ongoing challenge. BP nanosheets, phosphorus-based flame retardants, which can act in both gas and condensed-phase [25]. Besides the physical barrier effect, they can accelerate the carbonization and char formation of polymers. Specifically, the decomposition of BP releases phosphoric acid to promote cationic crosslinking, contributing to forming dense char [26], and then the dense char layer isolates the heat feedback to weaken polymer pyrolysis [27]. TOF nanosheets are generally synthesized by a condensation polymerization of melamine and cyanuric chloride through a facile solvothermal process. TOF may be a promising flame retardant for polymeric materials, taking into account the abundant nitrogen element and the large specific surface area of its 2D structure

Inspired by the outstanding physical and chemical properties of BP and TOF nanosheets, herein, the BP and TOF were creatively integrated to explore their synergistic effects on flame retardacy of epoxy resin. Specifically, functionalized BP nanosheets with NH_2 groups (BP-NH_2) were synthesized by urea-assisted ball-milling (Fig. S1). Then TOF was in situ grown on the surface of BP-NH_2 nanosheets through a facile solvothermal process, leading to the formation of BP-NH_2/TOF nanohybrids (BP-NH-TOF). The resultant BP-NH_2/TOF nanohybrids (BP-NH-TOF) with the rich amino groups on the surface may improve the compatibility between BP-NH-TOF and the epoxy matrix to significantly enhance the mechanical and flame retardancy. Mechanisms of flame retardant and mechanical reinforcement are investigated by various measurements. .

2. Experimental

The preparation of BP-NH-TOF nanosheets was achieved via one-pot solvothermal reaction (Fig. 1). The detailed information was shown in Supplementary Information, including raw materials, fabrication of BP-NH_2 nanosheets, BP-NH-TOF nanohybrid and EP/BP-NH-TOF nanocomposites and characterization.

3. Results and discussion

3.1. Characterization of BP-NH-TOF nanohybrid

In this work, a simple and efficient strategy to prepare BP-NH_2 nanosheets and BP-NH-TOF hybrids is proposed. As the initial template, $–NH_2$ functionalized BP nanosheets were synthesized by urea-assisted ball-milling. The morphology and structure of exfoliated BP-NH_2 were investigated by TEM. Exfoliated BP-NH_2 nanosheets show smooth surface with uniform brightness and several hundred nanometers in the diameter (Fig. 2a). The inserted figure is the electron diffraction pattern (SAED) of selected area for BP-NH_2 nanosheets, which is assigned to the orthogonal crystal structure of BP. The high-resolution TEM image of

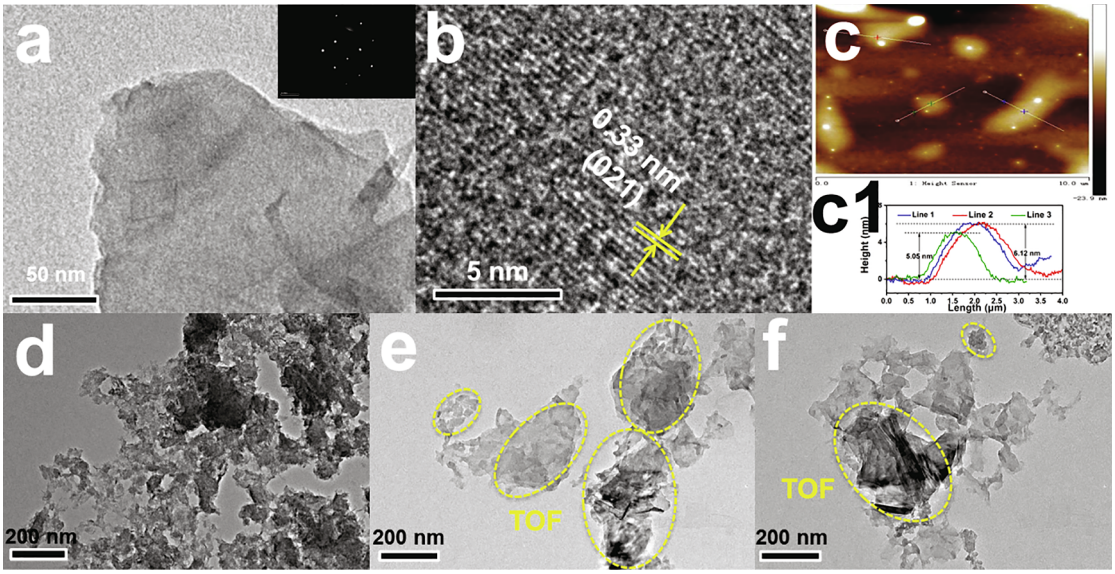

Fig. 2. Morphological characterization of BP-NH_2 and BP-NH-TOF nanosheets. (a) TEM image of the BP-NH_2 and (b) the corresponding high-resolution TEM image; (c) AFM image of BP-NH_2 nanosheets and (c1) the corresponding height profiles taken along the lines marked in; (d) TEM image of the TOF nanosheets; (e and f) TEM images of the BP-NH-TOF nanosheets.

BP-NH_2 nanosheets reflect a lattice spacing of 0.33 nm which is ascribed to (021) facet (Fig. 2b) [28]. The results demonstrate the complete retention of the lattice structure and the successful preparation of few-layer BP-NH_2 nanosheets. In order to confirm the specific thickness of few-layer BP-NH_2 nanosheets, atomic force microscopy (AFM) was conducted (Fig. 2c). BP-NH_2 nanosheets shows the thickness of 6.12 nm corresponding to 11–12 layers of P atoms based on the theoretical thickness of 0.53 nm for single-layer phosphorene [29].

As shown in Fig. 2d, the as-prepared TOF exhibits an irregular contour of up to tens of nanometers in size, and its surface with holes is different from BP-NH_2 nanosheets. Using the synthetic BP-NH_2 nanosheets as a template, TOF was polymerized in situ through a facile solvothermal process using melamine and cyanuric chloride as the raw materials. The morphology of BP-NH-TOF hybrid was investigated by TEM, as shown in Fig. 2e and f. The smooth sheets with a length of hundreds of nanometers are alleged to be BP-NH_2, while the fragmented shadow with tens of nanometers attached to the BP-NH_2 surface represents the TOF nanosheets. The successful preparation of sandwich structure for BP-NH-TOF hybrid with TOF nanosheets grown on the surface of BP-NH_2 nanosheets, which is verified by the size and morphology of nanomaterials In addition, the as-prepared BP-NH-TOF hybrid still maintains the nanosheets morphology well. Fig. S2b–e show the TEM images and the corresponding element mapping images of BP-NH-TOF nanohybrid, and the successful preparation of BP-NH-TOF nanohybrid was further confirmed via elemental mapping images of phosphorus, nitrogen and carbon respectively.

Fourier transform infrared spectroscopy (FTIR), Raman spectroscopy and X-Ray diffraction (XRD) were employed to further confirm the structures of BP-NH_2, TOF and BP-NH-TOF. For the FTIR spectrum of BP-NH-TOF hybrid (Fig. 3a), typical peaks, ascribing to BP-NH_2 and TOF nanosheets are identified. For instance, the peaks at 931, 1003, 1083, and 1161 cm^{-1} are attributed to P-N stretching vibration, P-O stretching vibration, P═O stretching vibration, rock vibration of NH_2 [11,30]. Moreover, the peak at 803 cm^{-1} is assigned to the s-triazine ring modes; the absorptions at 1255, 1332, 1448, and 1663 cm^{-1} are due to the typical aromatic CN heterocycle; the peak at 3228 cm^{-1} is attributed to the NH_2 vibration [31]. It is noted that the identifiable absorption peaks are weak and slightly shift compared with that of BP-NH_2 and TOF, which reveals the intensive hydrogen bonding interaction between TOF and BP-NH_2 nanosheets [11,32]. Fig. 3b shows the XRD pattern of the BP-NH-TOF hybrid. The typical diffraction peaks appearing at 17.1°, 26.6°, 34.3°, 35.2°, 52.5°, 56.2° and 56.8° correspond to (020), (021), (040), (111), (060), (151) and (061) interlayer planes of BP [33]. Furthermore, the broad peaks at 10.9°, 20.1°, 27.5°and a weaker peak at 40.1° are assigned to (010), (220), (001) and (002) planes of TOF, respectively [34]. The broad diffraction peaks indicate low crystallization and slight interlayer shift. All the diffraction peaks of BP-NH_2 and TOF nanosheets appear in the XRD pattern of BP-NH-TOF, indicating the successful preparation of TOF nanosheets via one pot solvothermal reaction using BP-NH_2 as a template. Fig. 3c shows the Raman spectrum of BP-NH-TOF hybrid. It can be seen that three vibration modes of A_g^1, B_{2g}, and A_g^2 caused by BP-NH_2 are located at 362.6, 438.9 and 467.3 cm^{-1} with the gradually rising baseline [30]. The rising baseline is mainly due to the fluorescence of TOF nanosheets on the surface of BP-NH_2, demonstrating the preservation of vibrational structure after the combination of BP-NH_2 and TOF nanosheets. In addition, the blue shift of vibration peaks occur in comparison to that of bulk BP (Fig. S3c), which reveals the few-layer BP-NH_2 nanosheets in BP-NH-TOF hybrid [11]. The surface area and pore size of TOF were investigated by nitrogen adsorption–desorption experiment, and the results are shown in Fig. 3d. The nitrogen adsorption–desorption isotherm curve of TOF belongs to the H3 hysteresis, which reveals the nanosheets structure of TOF with the BET surface of 37.7 m^2/g. The pore size distribution of TOF exhibits the sharp peak ranging from 3 to 4 nm and the broad peak centered at ~ 7.8 nm confirms mesoporous characteristics of TOF nanosheets.

The chemical composition and elemental valence state of BP-NH-TOF hybrid were characterized by XPS (Fig. 4). The XPS spectrum of BP-NH-TOF (Fig. 4a) shows the same elemental composition as TEM mapping (Fig. S2b–e). Fig. 4b reveals that the C 1 s spectrum of BP-NH-TOF can be deconvoluted into three peaks centered at 288.8, 286.1 and 284.8 eV, which are assigned to the sp^2-hybridized carbon (N–C═N), defect of sp^3 carbon (C–C) and aromatic sp^2 carbon, respectively [34,35]. The high-resolution N 1 s spectrum of BP-NH-TOF shows four intensive peaks at 401.1, 400.7, 400.2 and 399.2 eV (Fig. 4c), which are attributed to P-N bonds, amino function (C–N–H), tertiary nitrogen N-$(C)_3$ groups and sp^2-hybridized nitrogen in triazine rings (C–N═C) [11,34], respectively. For the P 2p spectrum of BP-NH-TOF (Fig. 4d), four peaks at 129.6 (P $2p_{3/2}$), 130.5 (P $2p_{1/2}$), 133.4 (P-N) and 134.4 eV (P-O) can be deconvoluted [11,36]. Noticeably, the binding energy of N 1 s peak for BP-NH-TOF is slightly higher than that of pristine TOF (Fig. S6), indicating the formation of interfacial interaction of hydrogen

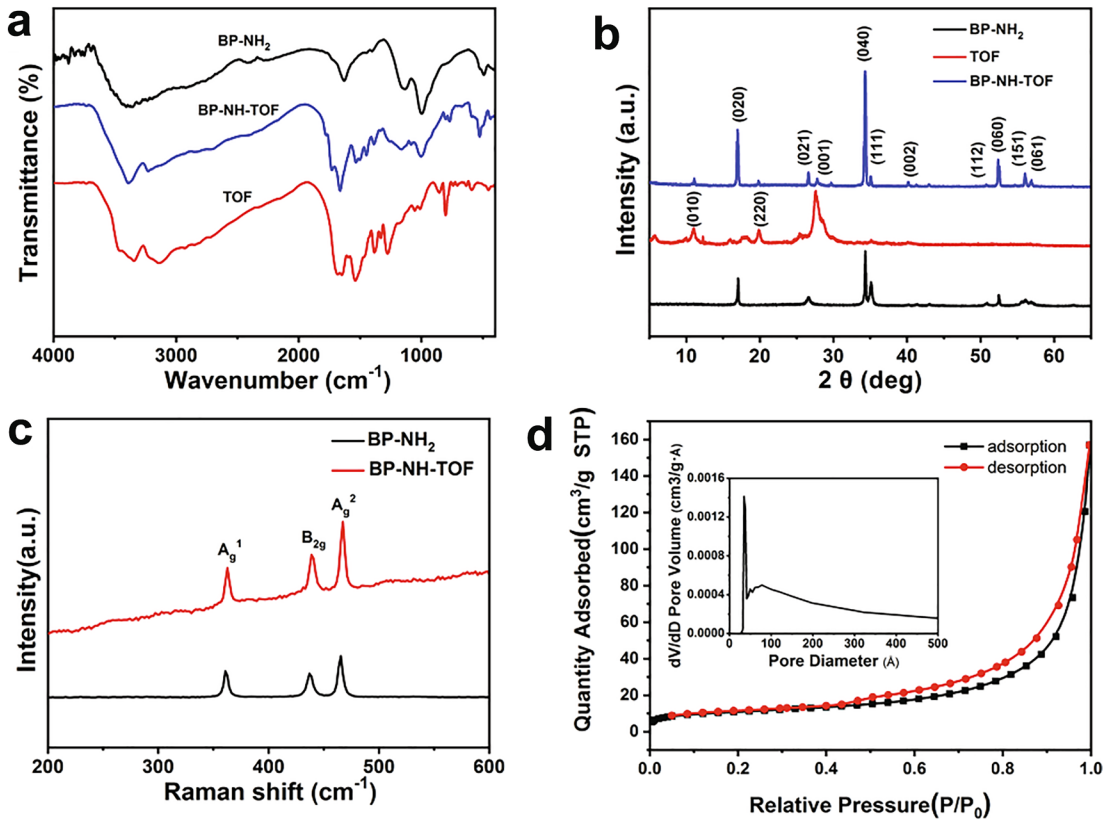

Fig. 3. (a) FTIR spectra and (b) XRD patterns of BP-NH_2, TOF and BP-NH-TOF; (c) Raman spectra of BP-NH_2 and BP-NH-TOF; (d) Nitrogen adsorption/desorption isotherm and pore size distribution curves of the TOF nanosheets.

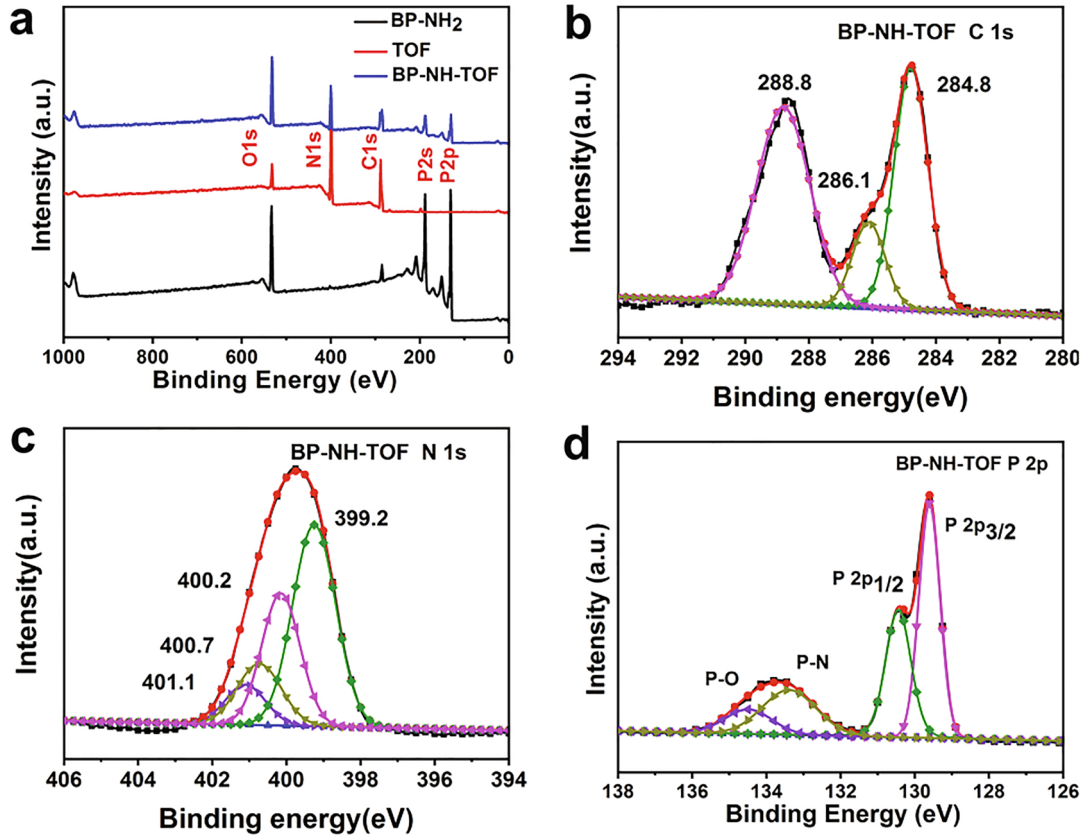

Fig. 4. (a) XPS survey spectra of BP-NH_2, TOF and BP-NH-TOF; High-resolution (d) C 1s, (e) N 1s and (f) P 2p XPS spectra of BP-NH-TOF.

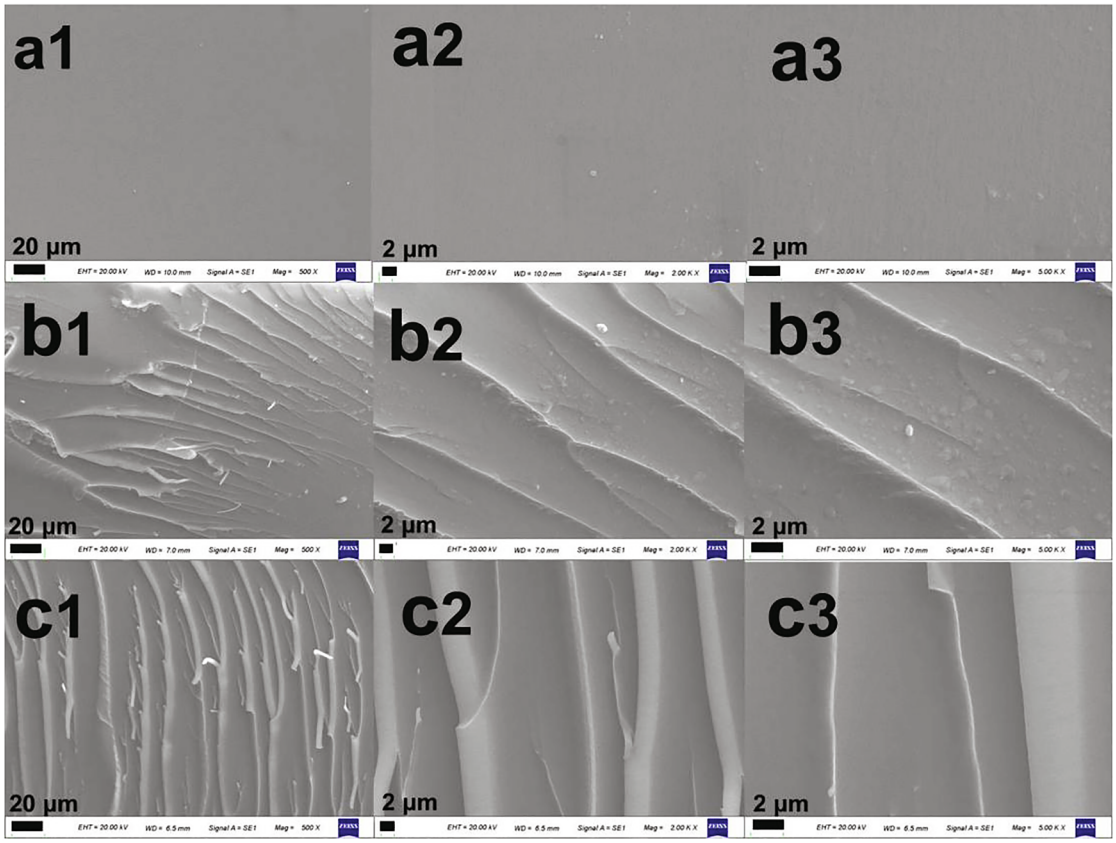

Fig. 5. SEM images of (a) pure EP, (b) EP/BP-$NH_2$2.0 and (c) EP/BP-NH-TOF2.0 at different magnifications.

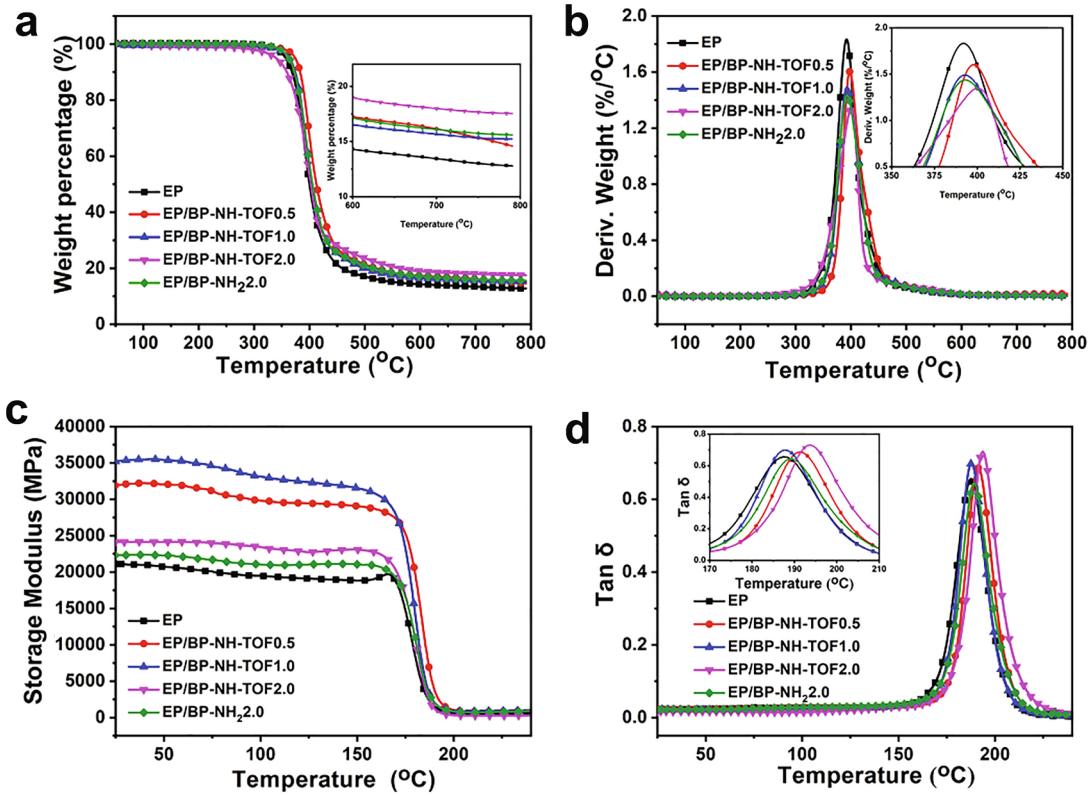

Fig. 6. (a) TGA and (b) DTG curves of pristine EP and its nanocomposites with different BP-NH-TOF contents; (c) Storage modulus (E') and (d) Tan δ curves of pure EP and its nanocomposites with different BP-NH-TOF contents as a function of temperature.

bonding between TOF and BP-NH_2 nanosheets. In summary, on the basis of the analysis results abovementioned, it can be concluded that TOF was successfully grown on the surface of NH_2-functionalized few-layer BP nanosheets.

3.2. Morphology and structure characterization of EP/BP-NH-TOF composites

Fig. 5 presents the SEM images of pristine EP, EP/BP-NH_2 + TOF2.0 and EP/BP-NH-TOF2.0 nanocomposites. For pure EP, the fractured surface exhibits a smooth, wrinkle-free morphology (Fig. 5a). The fractured surfaces of EP/BP-NH_2 (Fig. 5b) and EP/BP-NH_2 + TOF2.0 (Fig. S7) are relatively rough with small wrinkle, whereas the surface of EP/BP-NH-TOF2.0 (Fig. 5c) is the roughest and has a larger wrinkle pattern. This phenomenon indicates the formation of interface interaction between the nanofillers and EP matrix, resulting in the improved dispersion of BP-NH-TOF in EP matrix [37].

The XRD patterns of pristine EP, EP/BP-NH-TOF, EP/BP-$NH_2$2.0 and EP/BP-NH_2 + TOF2.0 are presented in Fig. S8. Compared with pure EP, there exist several sharp diffraction peaks in the XRD patterns of EP/BP-NH-TOF, EP/BP-$NH_2$2.0 and EP/BP-NH_2 + TOF2.0 composites, assigning to (020), (021), (040), (111), (112), (060), (151) and (061) interlayer planes of BP [33]. The characteristic peaks of TOF nanosheets are so weak that is nearly invisible, which is due to the small loading and low crystallization of TOF nanosheets. As a comparison, EP/BP-NH_2 + TOF2.0 show the typical peaks, but the intensity of the peak at ~ 35.2° corresponding to (111) plane which is significantly weaker than that of EP/BP-NH-TOF. Those phenomena verify that the hybridization with TOF can improve the dispersion of BP-NH-TOF in EP matrix.

3.3. Thermal and mechanical properties of EP and its composites

TGA have been widely employed to investigate thermal degradation behavior of materials [38,39]. The thermal stability of EP and its nanocomposites were analyzed by TGA under nitrogen (N_2), as shown in Fig. 6a and Fig. S9a. The $T_{-5\%}$, $T_{-50\%}$ and T_{max} are defined as the temperatures at 5%, 50% and maximum weight loss rate, and the corresponding parameters are listed in Table S3. EP and its nanocomposites show similar pyrolysis behavior with a one-stage mass loss process at the temperature ranging from 300 to 450 °C. Considering the thermal degradation of the BP-NH-TOF hybrid (Fig. S10), the un-decomposed BP-NH-TOF nanohybrids play a nano-barrier role during combustion. Furthermore, the incorporation of nanofillers leads to slightly early degradation of the corresponding EP nanocomposites, which is conductive to improving the flame retardancy [40]. It is noted that the final char yields of the EP nanocomposites at 800 °C are significantly increased. For example, the char yield of pristine EP is 12.8 wt%,while the char yields increase to 17.5 wt% as the BP-NH-TOF loading is increased to 2.0 wt%, which is higher than those of EP/BP-NH_2 (15.6 wt%) and EP/BP-NH_2 + TOF2.0 (15.2 wt%). The increased residues are beneficial to inhibiting the diffusion of pyrolysis products, and blocking the exchange of oxygen and heat to protect the underlying matrix during combustion. Fig. 6b and Table S3b show the derivative thermogravimetric (DTG) curves of EP and its nanocomposites. Pure EP has the maximum DTG value of 1.83%/°C, the mass loss rate of EP/BP-NH-TOF nanocomposites is significantly decreased. For example, the peak DTG value of EP/BP-NH-TOF2.0 is 1.34%/°C, which is lower than those of EP/BP-$NH_2$2.0 (1.44%/°C) and EP/BP-NH_2 + TOF2.0 (1.46%/°C). The significant decrease of thermal decomposition rate makes a crucial contribution to reducing the peak heat release rate (PHRR) of EP nanocomposites. It is noted that the EP/BP-NH_2 + TOF2.0 shows the earlier degradation than EP/BP-NH-TOF2.0, which is mainly caused by the low degradation temperature of TOF nanosheets (Fig. S10). In contrast, the hybridization of BP and TOF promotes the charring and inhibits the degradation of TOF. In summary, EP/BP-NH-TOF nanocomposites exhibit the increased char yield and significantly decreased mass loss rate, showing synergistic effect than the BP-$NH_2$2.0 or BP-NH_2 + TOF2.0 alone. This demonstrates that the hybridization of BP with TOF enhance the catalytic charring ability, demonstrating the synergistic physical barrier effect [41]. The well-designed P-N synergistic system promotes the formation of dense char layers, thus improving the flame retardancy of EP nanocomposites.

The influence of nanofillers on the dynamic thermo-mechanical properties of EP matrix was investigated by DMA. The storage modulus versus temperature curves of EP nanocomposites are shown in Fig. 6c and S9c. Error bars of storage modulus are given in Fig. S11. The storage modulus of pure EP is 21200 MPa at 25 °C, while that of EP/BP-NH-TOF nanocomposites are significantly increased by 51.4%, 67.1% and 14.4% at different BP-NH-TOF nanohybrid loadings of 0.5 wt%, 1.0 wt% and 2.0 wt%, respectively. The high stiffness of BP-NH_2 and the improved compatibility of TOF with the epoxy network via chemical bonding lead to enhanced storage modulus of the EP nanocomposites [31]. Unfortunately, the EP/BP-NH-TOF2.0 with higher loading shows worse performance than EP/BP-NH-TOF0.5 and EP/BP-NH-TOF1.0, which is mainly due to the agglomeration and uneven dispersion of BP-NH-TOF. In particular, the storage modulus of EP/BP-$NH_2$2.0 and EP/BP-NH_2 + TOF2.0 at 25 °C is 22.3 and 23.3 GPa, respectively, which are lower than those of EP/BP-NH-TOF (0.5 wt%, 1 wt%, 2.0 wt%), indicating that the hybridization of BP-NH_2 with TOF nanosheets can improve the interfacial interaction between BP-NH-TOF nanosheets and EP matrix. In addition, the peak of tan δ reflects the glass transition temperature (T_g) of the nanocomposites (Fig. 6d and S9d), which is gradually increased with the increase of BP-NH-TOF loading in the EP matrix. The significantly improved mechanical and thermal performance of EP/BP-NH-TOF nanocomposites is attributed to the enhanced interfacial interaction between the nanofiller and the matrix [31,32].

3.4. Flame retardancy of EP/BP-NH-TOF composites

Cone calorimeter could provide abundant information regarding combustion performance of materials, which correlates well with large-scale fire tests [42,43]. Fig. 7a and b present the heat release rate (HRR) and total heat release (THR) evolution of EP nanocomposites versus time. Various parameters obtained from cone calorimeter tests are listed in Table S4. Pure EP burns rapidly with high peak heat release rate (PHRR) and THR, which is 2053.4 kW/m^2 and 134.6 MJ/m^2, respectively. As the loading of BP-NH-TOF increases from 0.5 wt% to 2.0 wt%, the PHRR value of the corresponding EP nanocomposite is gradually decreased by 16.3% to 61.2%, while the THR value is decreased by 18.4% to 44.3%. Meanwhile, the PHRR and THR values of the EP/BP-$NH_2$2.0 are decreased by 46.8% and 40.7%, respectively. For EP nanocomposites containing BP-NH_2 and TOF at total loading of 2.0 wt% (Fig. S12a and b), the PHRR and THR values are decreased by 48.1% and 38.7%, respectively. Therefore BP-NH-TOF exhibits the highest flame retardancy efficiency. The smoke production rate (SPR) and total smoke release (TSR) vs. time curves of EP and its nanocomposites are shown in Fig. 7c and d. Pure EP releases a large amount of smoke during combustion, which is composed of polyaromatic hydrocarbon. As expected, with the introduction of BP-NH-TOF nanohybrid, the SPR and TSR values of nanocomposites are reduced significantly, and EP/BP-NH-TOF2.0 shows the lowest SPR and TSR values.

The limiting oxygen index (LOI) and the UL-94 vertical burning tests performance are critical to the prospect of EP composites application. The LOI refers to the concentration of the polymer in the mixed gas of oxygen and nitrogen that can just maintain the volume fraction of oxygen during combustion, which is very effective to judge the difficulty of combustion when the material is in contact with the flame. The LOI value of pure EP is 23.0%, manifesting the high flammability. After the incorporation of TOF, BP-NH_2, BP-NH-TOF and BP-NH_2 + TOF, the

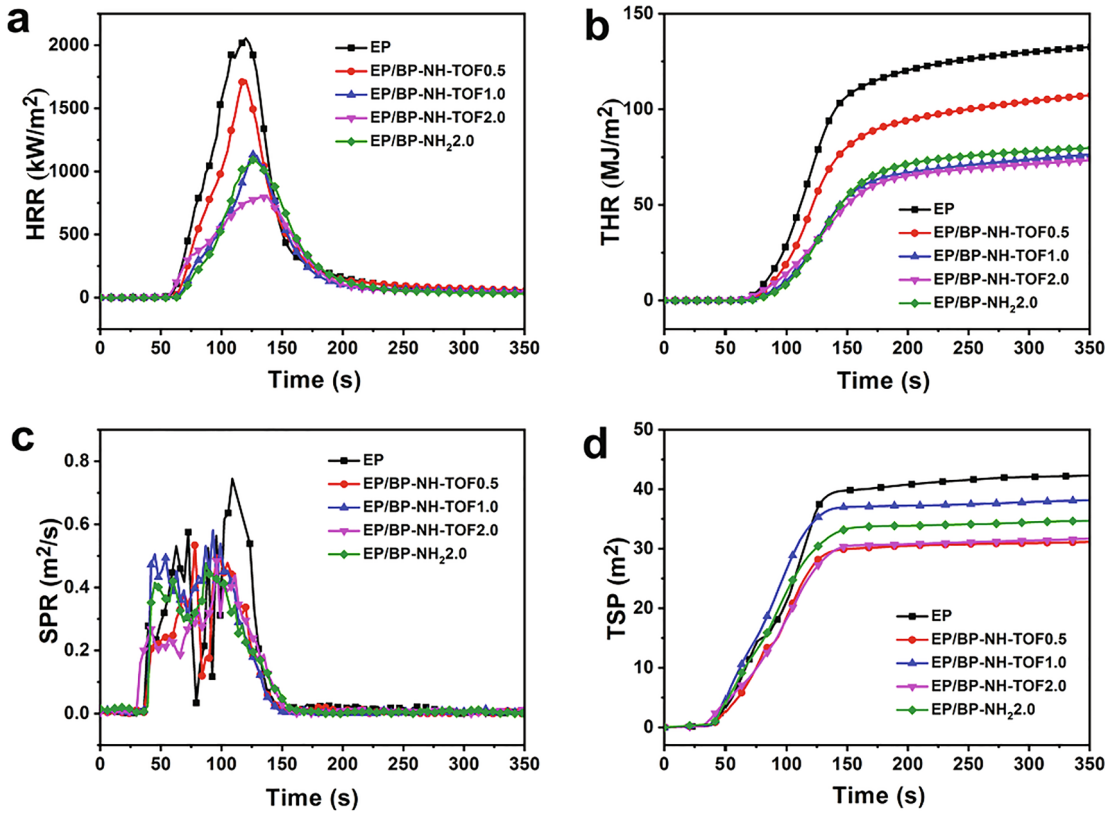

Fig. 7. (a) HRR, (b) THR, (c) SPR and (d) TSR curves of pure EP and its nanocomposites with different BP-NH-TOF contents obtained from cone calorimeter tests.

LOI values are increased. In particular, with the introduction of 2.0 wt% EP/BP-NH-TOF, the LOI value improved to 29.0%, which is higher than that of TOF, BP-NH_2 and BP-NH_2 + TOF with the same loading, and specific date is shown in Table S4. In terms of UL-94, a more intuitive and realistic scene of combustion behavior is shown, and the results are listed in Table S4. Actually, with the increasing loading of BP-NH-TOF in EP matrix, the results of UL-94 exhibit improved trend gradually. For instance, the improvement of EP/BP-NH-TOF 0.5 is not enough to meet the minimum standards of UL-94, the corresponding UL-94 level reaches V-1 rating while the addition of BP-NH-TOF reaching to 1.0 wt %. When the loading of BP-NH-TOF increased to 2.0 wt%, the composites pass the V-0 rating.

Considering the cone calorimeter, LOI and UL-94 results, EP/BP-NH-TOF2.0 shows the superior performance over other control samples. The enhanced fire safety property of EP nanocomposites is attributed to the physical barrier and catalytic charring effects of the BP-NH-TOF, a well-designed P-N synergistic flame retardant system.

3.5. Products analysis of EP/BP-NH-TOF nanocomposites

In order to explore the possible flame-retardant mechanism, degradation products of EP and its nanocomposites in the condensed phase and gas phase are identified respectively. Fig. 8 shows the char residues of EP nanocomposites after cone calorimeter tests. A small quantity of cracked char residues remain for pure EP (Fig. 8a). By contrast, the quantity and rigidness of char residues are gradually increased as the loading of BP-NH-TOF increases from 0.5 wt% to 2.0 wt % (Fig. 8b–d). The EP/BP-$NH_2$2.0 nanocomposite exhibits an expanded char layer with small holes on the surface (Fig. 8e), while the more continuous, denser expanded char layer is observed for EP/BP-NH-TOF2.0 nanocomposite (Fig. 8d). This phenomenon verifies that the hybridization of BP-NH_2 with TOF can improve the quality of char layer of EP nanocomposites. Fig. 9a–f shows the SEM images of the external and interior char residues of EP nanocomposites. The outer char layer of pure EP exhibits a sheet-like morphology with large open pores on the surface (Fig. 9a). In contrast, the external char layer of the EP/BP-$NH_2$2.0 shows a continuous and compact void-free surface (Fig. 9b). Similar to EP/BP-$NH_2$2.0, the EP/BP-NH-TOF2.0 nanocomposite has a continuous and dense char layer after combustion (Fig. 9c). Fig. 9d–f present the SEM images of the interior char layers. The internal char layer of the EP/BP-NH-TOF2.0 is more compact than pure EP and EP/BP-$NH_2$2.0. It can be observed that there are many large open pores on the surface of the internal char residues for pure EP and EP/BP-$NH_2$2.0. In contrast, the internal char of the EP/BP-NH-TOF has a more compact and tight wall with almost no holes. These phenomena indicate that the catalytic charring and physical barrier effect of BP-NH-TOF nanosheets are beneficial to the quality improvement of the final char layer. There is no doubt that a continuous dense carbon layer is beneficial to resisting the heat transfer, delaying the mass loss and suppressing the release of pyrolysis products, thereby improving the fire resistant performance. The ingredients and structure of char residues were evaluated by Raman spectroscopy. Two typical peaks at 1596 cm^{-1} (G band) and 1365 cm^{-1} (D band) can be observed in all the Raman spectra of EP, EP/BP-$NH_2$2.0 and EP/BP-NH-TOF2.0 (Fig. 9g–i). In general, the integrated intensity ratio of the D band to the G band (I_D/I_G) is employed to evaluate the degree of graphitization of char residues [44,45], and the higher I_D/I_G value reflects the lower degree of graphitization [30,39,46,47]. The I_D/I_G values of pristine EP, EP/BP-$NH_2$2.0 and EP/BP-NH-TOF2.0 are 3.23, 3.05 and 2.71, respectively. The EP/BP-NH-TOF2.0 has the lowest I_D/I_G value, indicating the highest degree of graphitization due to the catalytic charring effect of the BP-NH-TOF during combustion. The formation of char layer with higher carbonization degree is beneficial to preventing underlying materials from further degradation. Both XRD and XPS were utilized to characterize the structure and composition of the char residues of EP nanocomposite after cone calorimeter tests (Fig. 10). All the XRD patterns of the char residues for EP and its nanocomposites present a broad diffraction peak at $2\theta = 23^{\circ}$ (Fig. 10a), which is assigned to the (0 0 2)

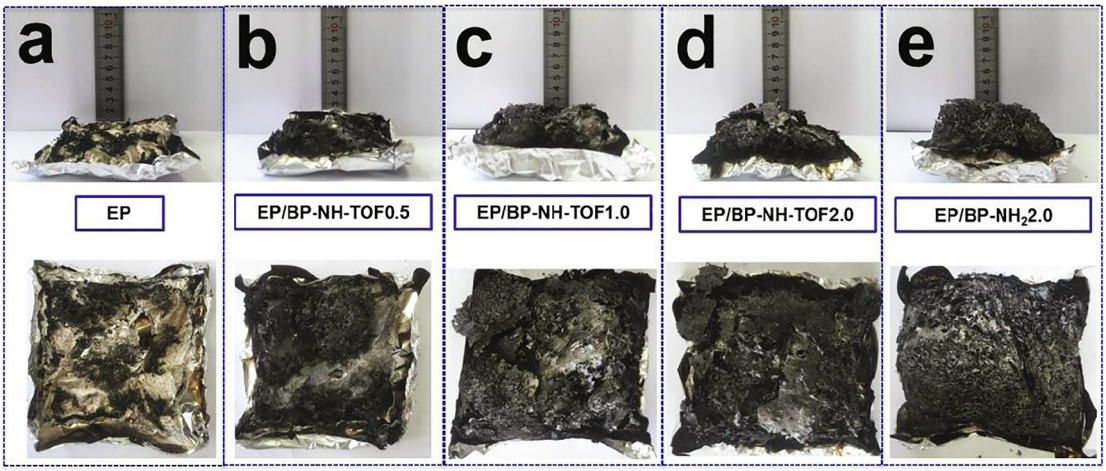

Fig. 8. Digital photos of the external residues from top view and side view for EP and its nanocomposites.

diffraction of carbon. Apart from the broad peak, there are no other diffraction peaks in the XRD patterns, demonstrating that the crystal structures of BP-NH_2 and TOF are destroyed during combustion. More detailed information on the char residues can be obtained from XPS results. The char residue of pure EP consists of O, N and C elements, and additional P element appears in the char residue of EP/BP-$NH_2$2.0 and EP/BP-NH-TOF nanocomposites (Fig. 10b). The high-resolution N 1s spectrum of EP/BP-NH-TOF presents three strong peaks at 401.1, 400.35 and 398.6 eV corresponding to P–N, C–N–C and C–N═C [11,34] (Fig. 10c). In addition, the High-resolution P 2p spectra of the char residues for EP/BP-$NH_2$2.0 and EP/BP-NH-TOF also further confirm the results (Fig. 10d and e). The P 2p peaks of EP/BP-$NH_2$2.0 and EP/BP-NH-TOF can be deconvoluted into three peaks at about 132.9, 133.8 and 134.65 eV corresponding to P–O–P, O–P═O and P_2O_5 bonds, respectively, which confirms the formation of char residue with phosphorus-nitrogen containing polyaromatic structure [48]. In summary, the BP-NH-TOF hybrids exhibit optimal synergistic charring effect to form continuous and compact char layer consisting of C, N, O and P. Therefore, the flame retardant mechanism in condensed phase is on the basis of the physical barrier effect of nanosheets and formed char layer.

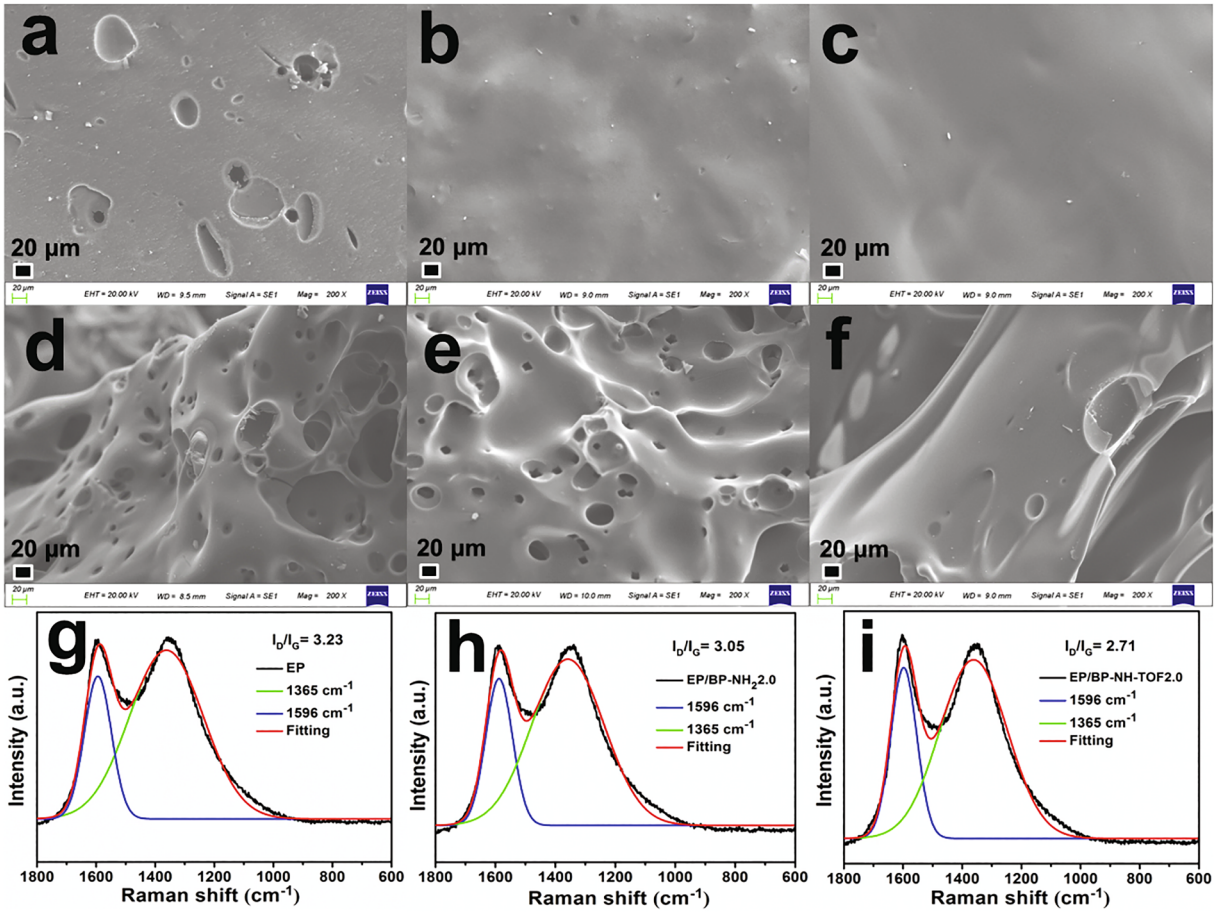

Fig. 9. SEM images of external (a–c), interior (d–f) char residues and Raman spectra of the char residues for pristine EP, EP/BP-$NH_2$2.0 and EP/BP-NH-TOF2.0.

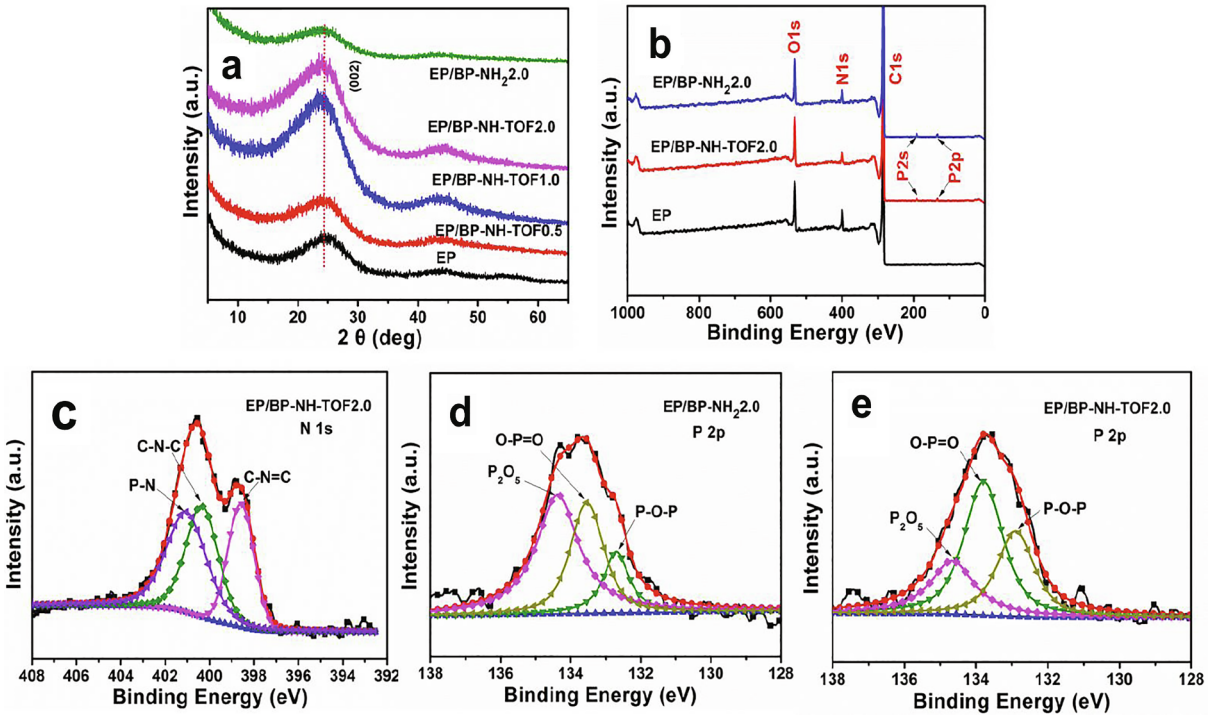

Fig. 10. (a) XRD patterns of the char residues for EP nanocomposites; (b) XPS survey spectra of the residual char for EP nanocomposites; (c) High-resolution N 1s spectra of the residues for EP/BP-NH-TOF2.0, P 2p spectra of the residues for (d) EP/BP-$NH_2$2.0 and (e) EP/BP-NH-TOF2.0.

For the purpose of exploring the action of EP/BP-NH-TOF in the gas phase, TG-FTIR technique was employed to investigate the pyrolysis products of EP, EP/BP-$NH_2$2.0 and EP/BP-NH-TOF2.0 nanocomposites (Fig. 11). Several typical peaks of pyrolysis products are located at 2930, 2360, 2190, 1740, and 1510 cm^{-1}, corresponding to hydrocarbons, carbon dioxide (CO_2), carbon monoxide (CO), carbonyl compounds, and aromatic compounds, respectively. The maximum absorption intensity of EP/BP-$NH_2$2.0 and EP/BP-NH-TOF2.0 is significantly reduced compared with pure EP. In particular, the EP/BP-NH-TOF2.0 nanocomposite shows the lowest absorption intensity of typical volatile products, which is in agreement with DTG results. The reduction of flammable pyrolysis products (including hydrocarbons, carbonyls and aromatics) are beneficial to reducing the release of heat and smoke. CO is considered to be the main toxic substance causing casualties in a fire, and the significant reduction of CO concentration contributes to the reduction of smoke toxicity and improvement of fire safety.

3.6. Flame retardant mechanism

EP/BP-NH-TOF nanocomposites show significantly enhanced flame retardancy properties. The reasonable flame retardancy mechanism of BP-NH-TOF is proposed based on systematically experimental results and prior works.

Two–stage thermal degradation is observed for EP [49]. The first stage is attributed to the decomposition of the matrix generating flammable gases, ignited under a suitable condition. The second stage is that the combustion heat feedback to the underlying polymer matrix, accelerating the further decomposition of the matrix to support gas-phase combustion. The repeated cycle of the two stages allows flame spread and development. BP-NH-TOF hybrids show the flame retardant action in both the condensed phase and gas phase. In condensed phase, undecomposed BP-NH-TOF acts as physical barrier in EP nanocomposites. In addition, BP-NH-TOF generates phosphorus species during thermal degradation, e.g. HPO_2 [50] which promote char formation and construct the three-dimensional (3D) expanded char layer. The undecomposed BP-NH-TOF and 3D char layer inhibit heat and oxygen transmission, preventing the further pyrolysis of underlying EP and reducing the release of flammable volatiles. In the gas phase, the generation of HO· and H· radicals are the key to the continuous combustion of polymeric materials. As an allotrope of solid phosphorus, the BP in EP matrix can generate PO· radicals during combustion, which can capture HO· and H· radicals in flame zone [51,52]. In addition, nitrogen-rich TOF can generate NH_3 during decomposition which dilutes the concentrations of flammable gases and creates an inert atmosphere to slow down combustion in the gas phase [53]. In summary, the significantly enhanced flame retardant performance of EP/BP-NH-TOF is attributed to the well-designed P-N flame retardatn system with the combination of physical barrier effect of nanosheets and char layer, and nonflammable gases dilution.

4. Conclusion

In this work, BP-NH_2 was synthesized by urea-assisted ball milling, which was used as a template to synthesize the BP/TOF nanohybrids by in-situ polycondensation. The composition and structure of BP-NH-TOF were well identified, which was subsequently incorporated into EP matrix. As the loading of BP-NH-TOF was increased, the char residue was increased along with the decrease in peak of DTG. In addition, the introduction of 2 wt% BP-NH-TOF led to 62.1% reduction in PHRR and up to 44.3% reduction in THR along with the dramatically enhanced LOI (29.0%) and UL-94 (V-0) properties, in addition to significantly reduced TSR and SPR values, indicting the outstanding flame retardancy performance. TG-FTIR results indicated that the amount of main toxic CO and flammable volatile products from thermal decomposition of EP nanocomposites were significantly inhibited, which meant the reduction of smoke production and heat release. In addition, EP/BP-NH-TOF behave better mechanical properties than pure EP, which was 67.1% increase in storage modulus at 1 wt% loading of BP-NH-TOF along with improved glass transition temperature. On the basis

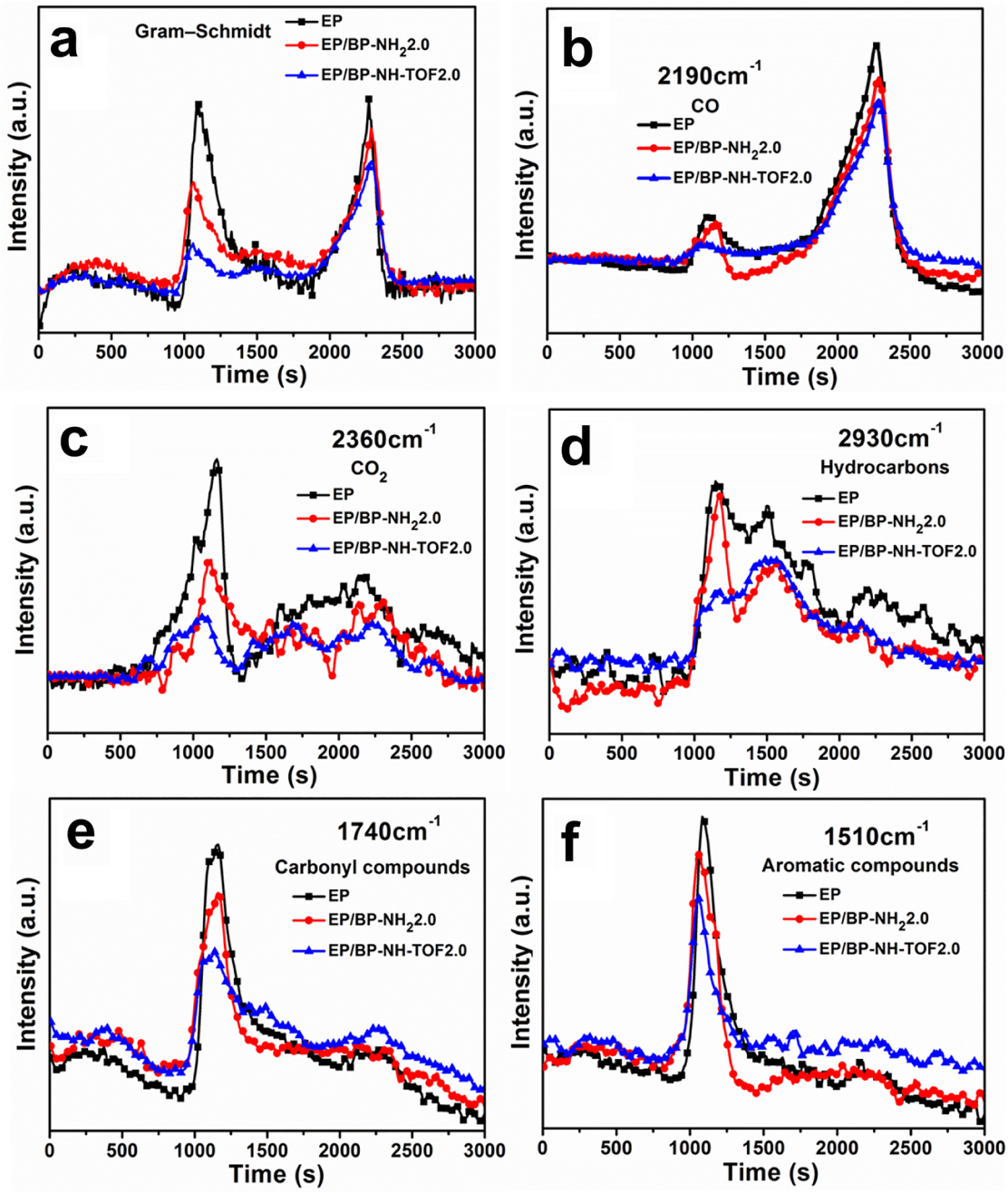

Fig. 11. Absorbance of pyrolysis products for EP, EP/BP-$NH_2$2.0 and EP/BP-NH-TOF2.0 vs. time: (a) total pyrolysis products, (b) CO, (c) CO_2, (d) hydrocarbons, (e) carbonyl compounds and (f) aromatic compounds.

of the analysis of the pyrolysis products and residues, the significant reduction of fire risk and enhanced mechanical properties are mainly due to the synergetic effect of BP-NH-TOF.

Author contributions

Shuilai Qiu and Bin Zou contributed equally to this work.

Declaration of interest statement

We declare that we have no financial and personal relationships with other people or organizations that can inappropriately influence our work.

Acknowledgements

This work was financially supported by the National Natural Science Foundation of China (51991352) and (51704269) and Fundamental Research Funds for the Central Universities (WK232-0000041, WK2320000043). The Atomic force microscopy (AFM) of BP-NH_2 was done in the Center for Micro- and Nanoscale Research and Fabrication of University of Science and Technology of China.

Appendix A. Supplementary data

Supplementary data to this article can be found online at https://doi.org/10.1016/j.cej.2020.126058.

References

[1] A. Castellanos-Gomez, Black phosphorus: narrow gap, wide applications, J. Phys. Chem. Lett. 6 (2015) 4280–4291.
[2] A. Carvalho, M. Wang, X. Zhu, A.S. Rodin, H. Su, A.H. Castro Neto, Phosphorene: from theory to applications, Nat. Rev. Mater. 1 (2016) 16061.
[3] A. Carvalho, M. Wang, X. Zhu, A.S. Rodin, H. Su, A.H.C. Neto, Phosphorene: from theory to applications, Nat. Rev. Mater. 1 (2016) 1–16.
[4] A. Khandelwal, K. Mani, M.H. Karigerasi, I. Lahiri, Phosphorene-The two-dimensional black phosphorous: properties, synthesis and applications, Mater. Sci. Eng., B 221 (2017) 17–34.
[5] M. Batmunkh, M. Bat-Erdene, J.G. Shapter, Phosphorene and phosphorene-based materials-prospects for future applications, Adv. Mater. 28 (2016) 8586–8617.
[6] X. Ling, H. Wang, S. Huang, F. Xia, M.S. Dresselhaus, The renaissance of black phosphorus, 112 (2015) 4523-4530.
[7] Q. Jiang, L. Xu, N. Chen, H. Zhang, L. Dai, S. Wang, Facile Synthesis of Black Phosphorus: an Efficient Electrocatalyst for the Oxygen Evolving Reaction, Angewandte Chemie-International Edition 55 (2016) 13849–13853.
[8] X. Ren, J. Zhou, X. Qi, Y. Liu, Z. Huang, Z. Li, Y. Ge, S.C. Dhanabalan, J.S. Ponraj, S. Wang, J. Zhong, H. Zhang, Few-layer black phosphorus nanosheets as electrocatalysts for highly efficient oxygen evolution reaction, Adv. Energy Mater. 7 (2017).
[9] Z. Shen, S. Sun, W. Wang, J. Liu, Z. Liu, J.C. Yu, A black-red phosphorus heterostructure for efficient visible-light-driven photocatalysis, J. Mater. Chem. A 3 (2015) 3285–3288.
[10] X. Zhu, T. Zhang, Z. Sun, H. Chen, J. Guan, X. Chen, H. Ji, P. Du, S. Yang, Black phosphorus revisited: a missing metal-free elemental photocatalyst for visible light hydrogen evolution, Adv. Mater. 29 (2017) 1605776.
[11] L. Shao, H. Sun, L. Miao, X. Chen, M.o. Han, J. Sun, S. Liu, L. Li, F. Cheng, J. Chen, Facile preparation of NH 2 -functionalized black phosphorene for the electrocatalytic hydrogen evolution reaction, J. Mater. Chem. A 6 (6) (2018) 2494–2499.
[12] N.A. Zwaneveld, R. Pawlak, M. Abel, D. Catalin, D. Gigmes, D. Bertin, L. Porte, Organized formation of 2D extended covalent organic frameworks at surfaces, J. Am. Chem. Soc. 130 (2008) 6678–6679.
[13] E.L. Spitler, M.R. Giovino, S.L. White, W.R. Dichtel, A mechanistic study of Lewis acid-catalyzed covalent organic framework formation, Chem. Sci. 2 (2011) 1588–1593.
[14] M.J. Bojdys, J. Jeromenok, A. Thomas, M.J.A.m. Antonietti, Rational extension of the family of layered, covalent, triazine-based frameworks with regular porosity, 22 (2010) 2202-2205.
[15] S. Ren, M.J. Bojdys, R. Dawson, A. Laybourn, Y.Z. Khimyak, D.J. Adams, A.I.J.A.M. Cooper, Porous, fluorescent, covalent triazine-based frameworks via room-temperature and microwave-assisted, Synthesis 24 (2012) 2357–2361.
[16] R. Gomes, P. Bhanja, A. Bhaumik, A triazine-based covalent organic polymer for efficient CO2 adsorption, Chem. Commun. 51 (2015) 10050–10053.
[17] P. Wen, C. Zhang, Z. Yang, R. Dong, D. Wang, M. Fan, J. Wang, Triazine-based covalent-organic frameworks: a novel lubricant additive with excellent tribological performances, Tribol. Int. 111 (2017) 57–65.
[18] A.P. Côté, A.I. Benin, N.W. Ockwig, M. O'Keeffe, A.J. Matzger, O.M. Yaghi, Porous, Crystalline, Covalent Organic Frameworks, 310 (2005) 1166-1170.
[19] X. Feng, X. Ding, D. Jiang, Covalent organic frameworks, Chem. Soc. Rev. 41 (2012) 6010–6022.
[20] S.-Y. Ding, W. Wang, Covalent organic frameworks (COFs): from design to applications, Chem. Soc. Rev. 42 (2013) 548–568.
[21] P. Puthiaraj, Y.-R. Lee, S. Zhang, W.-S.J.J.o.M.C.A. Ahn, Triazine-based covalent organic polymers: design, synthesis and applications in heterogeneous catalysis 4 (2016) 16288-16311.
[22] R.C. Hale, M.J. La Guardia, E.P. Harvey, M.O. Gaylor, T.M. Mainor, W.H. Duff, Persistent pollutants in land-applied sludges, Nature 412 (2001) 140–141.
[23] E.D. Schreder, M.J.J.E.s. La Guardia, technology, Flame retardant transfers from US households (dust and laundry wastewater) to the aquatic environment 48 (2014) 11575-11583.
[24] T. Mayer-Gall, D. Knittel, J.S. Gutmann, K.J.A.a.m. Opwis, interfaces, Permanent flame retardant finishing of textiles by allyl-functionalized polyphosphazenes, 7 (2015) 9349-9363.
[25] S. Qiu, Y. Zhou, X. Zhou, T. Zhang, C. Wang, R.K. Yuen, W. Hu, Y.J.S. Hu, Air-stable polyphosphazene-functionalized few-layer black phosphorene for flame retardancy of epoxy, Resins 15 (2019) 1805175.
[26] B. Zou, S. Qiu, X. Ren, Y. Zhou, F. Zhou, Z. Xu, Z. Zhao, L. Song, Y. Hu, X.J.J.o.h.m. Gong, Combination of black phosphorus nanosheets and MCNTs via phosphorus-carbon bonds for reducing the flammability of air stable epoxy resin nanocomposites 383 (2020) 121069.
[27] R. Ball, A. McIntosh, J. Brindley, The role of char-forming processes in the thermal decomposition of cellulose, PCCP 1 (1999) 5035–5043.
[28] L.-Q. Sun, M.-J. Li, K. Sun, S.-H. Yu, R.-S. Wang, H.-M.J.T.J.o.P.C.C. Xie, Electrochemical activity of black phosphorus as an anode material for lithium-ion batteries 116 (2012) 14772-14779.
[29] X. Wang, A.M. Jones, K.L. Seyler, T. Vy, Y. Jia, H. Zhao, H. Wang, L. Yang, X. Xu, F. Xia, Highly anisotropic and robust excitons in monolayer black phosphorus, Nat. Nanotechnol. 10 (2015) 517–521.
[30] A. Ambrosi, Z. Sofer, M.J.A.C.I.E. Pumera, Electrochemical Exfoliation of Layered Black Phosphorus into Phosphorene, 56 (2017) 10443-10445.
[31] X. Mu, J. Zhan, X. Feng, B. Yuan, S. Qiu, L. Song, Y. Hu, Novel melamine/o-phthalaldehyde covalent organic frameworks nanosheets: enhancement flame retardant and mechanical performances of thermoplastic polyurethanes, ACS Appl. Mater. Interfaces 9 (2017) 23017–23026.
[32] Y. Ti, Q. Wen, D. Chen, Characterization of the hydrogen bond in polyurethane/attapulgite nanocomposites, 133 (2016).
[33] Q. Jiang, L. Xu, N. Chen, H. Zhang, L. Dai, S.J.A.C.I.E. Wang, Facile synthesis of black phosphorus: an efficient electrocatalyst for the oxygen evolving reaction, 55 (2016) 13849-13853.
[34] P. Wen, C. Zhang, Z. Yang, R. Dong, D. Wang, M. Fan, J.J.T.I. Wang, Triazine-based covalent-organic frameworks: A novel lubricant additive with excellent tribological performances, 111 (2017) 57-65.
[35] J. Wang, D. Zhang, Y. Zhang, W. Cai, C. Yao, Y. Hu, W. Hu, Construction of multifunctional boron nitride nanosheet towards reducing toxic volatiles (CO and HCN) generation and fire hazard of thermoplastic polyurethane, J. Hazard. Mater. 362 (2019) 482–494.
[36] J. Plutnar, J. Šturala, V. Mazánek, Z. Sofer, M.J.A.F.M. Pumera, Fluorination of Black Phosphorus—Will Black Phosphorus Burn Down in the Elemental Fluorine? 28 (2018) 1801438.
[37] L. Yang, S.L. Phua, J.K.H. Teo, C.L. Toh, S.K. Lau, J. Ma, X. Lu, A biomimetic approach to enhancing interfacial interactions: polydopamine-coated clay as reinforcement for epoxy resin, ACS Appl. Mater. Interfaces 3 (2011) 3026–3032.
[38] Y. Shi, C. Liu, L. Liu, L. Fu, B. Yu, Y. Lv, F. Yang, P. Song, Strengthening, toughing and thermally stable ultra-thin MXene nanosheets/polypropylene nanocomposites via nanoconfinement, Chem. Eng. J. 378 (2019) 122267.
[39] Y. Shi, B. Yu, Y. Zheng, J. Yang, Z. Duan, Y. Hu, Design of reduced graphene oxide decorated with DOPO-phosphanomidate for enhanced fire safety of epoxy resin, J. Colloid Interface Sci. 521 (2018) 160–171.
[40] W. Guo, B. Yu, Y. Yuan, L. Song, Y. Hu, In situ preparation of reduced graphene oxide/DOPO-based phosphonamidate hybrids towards high-performance epoxy nanocomposites, Compos. B Eng. 123 (2017) 154–164.
[41] Z. Qu, K. Wu, E. Jiao, W. Chen, Z. Hu, C. Xu, J. Shi, S. Wang, Z. Tan, Surface functionalization of few-layer black phosphorene and its flame retardancy in epoxy resin, Chem. Eng. J. 122991 (2019).
[42] B. Lin, A.C.Y. Yuen, A. Li, Y. Zhang, T.B.Y. Chen, B. Yu, E.W.M. Lee, S. Peng, W. Yang, H.-D. Lu, MXene/chitosan nanocoating for flexible polyurethane foam towards remarkable fire hazards reductions, J. Hazard. Mater. 381 (2020) 120952.
[43] B. Yu, B. Tawiah, L.-Q. Wang, A.C.Y. Yuen, Z.-C. Zhang, L.-L. Shen, B. Lin, B. Fei, W. Yang, A. Li, Interface decoration of exfoliated MXene ultra-thin nanosheets for fire and smoke suppressions of thermoplastic polyurethane elastomer, J. Hazard. Mater. 374 (2019) 110–119.
[44] X. Zhou, S. Qiu, W. Xing, C.S.R. Gangireddy, Z. Gui, Y. Hu, Hierarchical polyphosphazene@molybdenum disulfide hybrid structure for enhancing the flame retardancy and mechanical property of epoxy resins, ACS Appl. Mater. Interfaces 9 (2017) 29147–29156.
[45] Z. Zhao, W. Cai, Z. Xu, X. Mu, X. Ren, B. Zou, Z. Gui, Y. Hu, Multi-role p-styrene sulfonate assisted electrochemical preparation of functionalized graphene nanosheets for improving fire safety and mechanical property of polystyrene composites, Compos. B Eng. 181 (2020) 107544.
[46] W. Cai, X. Feng, B. Wang, W. Hu, B. Yuan, N. Hong, Y. Hu, A novel strategy to simultaneously electrochemically prepare and functionalize graphene with a multifunctional flame retardant, Chem. Eng. J. 316 (2017) 514–524.
[47] B. Yu, W. Xing, W. Guo, S. Qiu, X. Wang, S. Lo, Y. Hu, Thermal exfoliation of hexagonal boron nitride for effective enhancements on thermal stability, flame retardancy and smoke suppression of epoxy resin nanocomposites via sol–gel process, J. Mater. Chem. A 4 (2016) 7330–7340.
[48] C. Gibaja, D. Rodriguez-San-Miguel, P. Ares, J. Gómez-Herrero, M. Varela, R. Gillen, J. Maultzsch, F. Hauke, A. Hirsch, G. Abellán, Few-layer antimonene by liquid-phase exfoliation, Angew. Chem. Int. Ed. 55 (2016) 14345–14349.
[49] K.L.J.J.o.T.A. Erickson, Calorimetry, Thermal decomposition mechanisms common to polyurethane, epoxy, poly(diallyl phthalate), polycarbonate and poly(phenylene sulfide) 89 (2007) 427-440.
[50] A. König, E. Kroke, Flame retardancy working mechanism of methyl-DOPO and MPPP in flexible polyurethane foam, 36 (2012) 1-15.
[51] O.P. Korobeinichev, V.M. Shvartsberg, A.G. Shmakov, T.A. Bolshova, T.M. Jayaweera, C.F. Melius, W.J. Pitz, C.K. Westbrook, H. Curran, Flame inhibition by phosphorus-containing compounds in lean and rich propane flames, Proc. Combust. Inst. 30 (2005) 2353–2360.
[52] F. Zhou, T. Zhang, B. Zou, W. Hu, B. Wang, J. Zhan, C. Ma, Y. Hu, Synthesis of a novel liquid phosphorus-containing flame retardant for flexible polyurethane foam: combustion behaviors and thermal properties, Polym. Degrad. Stab. 171 (2020) 109029.
[53] W.K.P. Lim, M. Mariatti, W.S. Chow, K.T. Mar, Effect of intumescent ammonium polyphosphate (APP) and melamine cyanurate (MC) on the properties of epoxy/glass fiber composites, Compos. Part B-Eng. 43 (2012) 124–128.